PNAS RESEARCH ARTICLE | ENGINEERING

Effect of local chemical order on the irradiation-induced defect evolution in CrCoNi medium-entropy alloy

Zhen Zhang[a,1], Zhengxiong Su[b,1], Bozhao Zhang[a,1], Qin Yu[c], Jun Ding[a,2], Tan Shi[b], Chenyang Lu[b,2], Robert O. Ritchie[c,d], and Evan Ma[a,2]

Edited by Alexis Bell, University of California, Berkeley, CA; received November 1, 2022; accepted February 27, 2023

High- (and medium-) entropy alloys have emerged as potentially suitable structural materials for nuclear applications, particularly as they appear to show promising irradiation resistance. Recent studies have provided evidence of the presence of local chemical order (LCO) as a salient feature of these complex concentrated solid-solution alloys. However, the influence of such LCO on their irradiation response has remained uncertain thus far. In this work, we combine ion irradiation experiments with large-scale atomistic simulations to reveal that the presence of chemical short-range order, developed as an early stage of LCO, slows down the formation and evolution of point defects in the equiatomic medium-entropy alloy CrCoNi during irradiation. In particular, the irradiation-induced vacancies and interstitials exhibit a smaller difference in their mobility, arising from a stronger effect of LCO in localizing interstitial diffusion. This effect promotes their recombination as the LCO serves to tune the migration energy barriers of these point defects, thereby delaying the initiation of damage. These findings imply that local chemical ordering may provide a variable in the design space to enhance the resistance of multi-principal element alloys to irradiation damage.

local chemical order | medium-entropy alloy | irradiation-induced defects | point defects

Significance

High-entropy alloys have emerged as promising structural materials for nuclear applications. Among the structural features of high-entropy alloys that may influence their irradiation response, a variable that has not received careful study so far is the internal local chemical order. By combining ion irradiation experiments and atomistic simulation of CrCoNi medium-entropy alloy, here we demonstrate that increased local chemical order (e.g., via thermal aging) significantly enhances their resistance to irradiation damage by narrowing the mobility ratio of irradiation-induced interstitials and vacancies that can facilitate their recombination. This finding opens an avenue to tailor radiation resistance, especially effective as the local chemical order are well suited to affect the evolution of point defects.

High-entropy (HEAs) and medium-entropy (MEAs) alloys, denoted as M/HEAs, have attracted considerable attention due to their exceptional mechanical properties (1, 2) and corrosion resistance (3, 4). Recent studies have also demonstrated that M/HEAs have potential to be used as candidate materials for advanced nuclear applications since they exhibit improved irradiation resistance (5–8). To date, both experimental studies and atomistic simulations have been carried out to investigate the irradiation behavior of M/HEAs. Specifically, extensive experimental studies have focused on tuning chemical complexities to enhance radiation tolerance in concentrated solid-solution alloys, by varying the number, the type, and the concentration of principal elements (9). Manipulation of these constituent elements can provide an effective approach to alter the lattice distortion and consequently control the process of defect production and recombination, which could ultimately suppress damage accumulation. For instance, increasing the number of alloying elements has been shown to modify defect migration pathways in Ni-based single-phase face-centered cubic (*fcc*) equiatomic alloys from a one- to three-dimensional (3-D) mode, which would enhance the probability of the recombination of irradiation-induced vacancies and interstitials, and hence reduce the residual defect concentration in the alloy (5, 7).

Concurrently, atomistic simulations have also been employed to shed light on the primary damage processes in M/HEAs (8, 10–12). However, conclusive evidence is still lacking as to whether M/HEAs in general possess superior irradiation tolerance for specific primary damage processes. A recent molecular dynamics (MD) study by Lin et al. (8) demonstrated the CrFeCoNi HEA to be more irradiation tolerant than pure Ni. The delayed damage accumulation in the HEA was attributed to a higher recombination of defects caused by the enhanced thermal spike (i.e., increased recombination probability between vacancies and interstitials), the lower thermal conductivity, and the substantially smaller binding energies of defect clustering in the HEA compared to pure Ni. Deluigi et al. (12) simulated the evolution of defects during primary irradiation damage and found essentially the same results in the CrFeCoNiCu HEA as in pure Ni. Based on these findings, these authors proposed that the origin of the radiation resistance in HEAs that has been observed experimentally may not be related to a reduction in primary damage due to chemical disorder, but rather involves the longer times required for defect evolution.

On the basis of these previous studies (5–12), the enhanced irradiation tolerance of M/HEAs has been usually correlated to effects that are invariably associated with their compositional complexity, such as their reduced thermal conductivities, sluggish diffusion, and lattice distortion although some of the proposed mechanisms are still under debate,

Author contributions: J.D., C.L., and E.M. designed research; Z.Z., Z.S., B.Z., Q.Y., and J.D. performed research; Z.Z., Z.S., B.Z., J.D., T.S., C.L., R.O.R., and E.M. analyzed data; and Z.Z., Z.S., B.Z., Q.Y., J.D., C.L., R.O.R., and E.M. wrote the paper.

The authors declare no competing interest.

This article is a PNAS Direct Submission.

[1]Z.Z., Z.S., and B.Z. contributed equally to this work.

[2]To whom correspondence may be addressed. Email: dingsn@xjtu.edu.cn, chenylu@xjtu.edu.cn, or maen@xjtu.edu.cn.

This article contains supporting information online at https://www.pnas.org/lookup/suppl/doi:10.1073/pnas.2218673120/-/DCSupplemental.

Published April 4, 2023.

as discussed in a recent review (13). Local chemical order (LCO) has also been identified as yet another prominent characteristic of multi-principal element alloys (14–16). Indeed, it has been proposed that such local ordering may be highly tunable by changing the alloy processing conditions, and further that its presence can strongly influence the energetics of defect formation, dislocation mobility, and slip mode, and hence influence the mechanical behavior of these materials (17–21). Only very recently have numerical simulations been attempted to investigate the influence of LCO on the radiation tolerance of M/HEAs (22–24). However, the specific effect of LCO on the evolution of radiation-induced defects in M/HEAs has not been experimentally validated nor carefully explored, not to mention an in-depth understanding.

In this work, we combine in situ He^+ irradiation experiments with atomistic simulations of primary damage to uncover the influence of LCO on the response of the equiatomic CrCoNi MEA to ion irradiation. This alloy is a representative of the *fcc* multi-principal element systems with mechanical properties that are mechanistically typical of other single-phase, solid-solution HEAs (25). In fact, its strength, ductility, and toughness properties are among the best on record (2), with a room-temperature radiation resistance comparable to that of CrFeCoNi and far superior to that of CoNi and pure Ni (6, 26). Our objective here is to compare the irradiation response of as-prepared CrCoNi (hereafter approximated as a random solid solution, RSS) with an annealed and aged CrCoNi with a heightened degree of LCO (termed LCO CrCoNi); pure Ni is additionally simulated for comparison. Our results demonstrate that the presence of LCO does make a difference in the formation and evolution of the defects in the CrCoNi alloy upon irradiation. As local chemical ordering appears to be tunable, for example via heat treatment, this provides a fascinating avenue for the development of irradiation-resistant M/HEAs better suited for nuclear applications.

Results and Discussion

Irradiation Experiments. In the experimental part of this study, we focus on the CrCoNi alloy processed with different heat treatments following homogenization at 1,200 °C, specifically water quenching from 1,200 °C to form an RSS CrCoNi, versus aging at 1,000 °C for 120 h followed by slow furnace cooling to create the LCO CrCoNi condition. The latter heat treatment has been shown, using energy-filtered transmission electron microscopy (TEM) (14), to induce LCO in the form of nanometer-scale domains; details of the sample preparation are given in the *Methods*. Here, we provide additional experimental evidence for the existence of chemical short-range order (CSRO) in the CrCoNi alloy after annealing, following the Cs-corrected TEM approach that has recently been successfully utilized to reveal CSRO in a *fcc* VCoNi MEA (15) and a CrCoNi MEA (16). This method is mainly based on atomic high-angle annual dark field (HAADF) imaging under the [112] zone axis, see Fig. 1 *A* and *D* . The size and distribution of CSRO are obtained by inverse fast Fourier transform (IFFT) of the diffraction disks (1/2{3_11}) arising from the CSRO, see Fig. 1 *C* and *F*. In addition, the diffraction intensity along the orange dashed line in Fig. 1*A* and *C* is shown in Fig. 1*B* and *E*, respectively, and the red arrows indicate the extra intensity at 1/2 {3_11} positions. More technical details can be found in the *Methods* and refs. (15, 16).

We note that the CSRO as determined from the TEM images (highlighted by the red circles in Fig. 1 *C* and *F*) is consistent with the previous identification (15, 16), where detailed chemical mapping information about the CSRO has been provided. Fig. 1*G* shows that the CSRO regions (i.e., LCO in the form of CSRO, with partial chemical order developed only to the nearest-neighbor atomic shells) have an average diameter of around 0.5 nm (the mean CSRO size in the 1,000 °C-aged sample is slightly larger than that in the water-quenched one as reflected by the fat tail in the distribution profile of the annealed sample). In comparison, the 1,000 °C-aged sample contains significantly more CSRO than the water-quenched sample. The areal fraction of the LCO regions estimated from the images is about 3% in the water-quenched CrCoNi, whereas this value is as much as about 30% in the annealed CrCoNi, see Fig. 1*H*. Based on these TEM characterizations, we conclude that the amount of LCO in the water-quenched CrCoNi alloy is negligible, and thus, it can be rightfully approximated as a RSS. By contrast, the 1,000 °C-aged sample contains a notable content of LCO, and thus, it is reasonable to term this alloy as LCO CrCoNi.

Both the RSS and LCO CrCoNi alloys were then in situ ion irradiated with 50 keV He^+ ions; details are described in the *Methods*. The depth profiles of displacements per atom (dpa) and the helium concentration for the CrCoNi alloy with 50 keV He^+ irradiation were calculated using the SRIM software (27) in quick Kinchin–Pease mode with a displacement threshold energy of 40 eV for all elements, as shown in *SI Appendix*, Fig. S1.

Fig. 2 presents TEM images of both the water-quenched (RSS) and 1,000 °C-aged (LCO) CrCoNi alloys after various irradiation doses (0.16 to 1.0 dpa). The number density of the small dots (white in TEM weak beam dark-field), which have been identified as small stacking-fault tetrahedra (SFT) or precursors of loops (28, 29), gradually increases with increasing irradiation dose. A closer look at these irradiation-induced defect clusters with scanning transmission electron microscopy (STEM) bright-field (BF) imaging in Fig. 3 *A* and *B* indeed reveals the presence of SFT and 1/3<111> dislocation loops in the RSS CrCoNi sample after irradiation. As shown in Fig. 2, at the low doses of irradiation, such as 0.16 dpa, some defect clusters (white dots) are already present in the water-quenched RSS sample, whereas the corresponding 1,000 °C-aged LCO sample is nearly defect free. With increasing irradiation dose, progressively more defect clusters appear in both the water-quenched RSS and 1,000 °C-aged LCO samples, although the latter always exhibits a smaller number density. Such observations indicate that the presence of LCO can effectively inhibit the formation of defect clusters in the early stage of irradiation (up to 1.0 dpa).

Quantitatively, the average size and number density of the irradiation-induced defect clusters in the RSS and LCO CrCoNi samples at different irradiation doses are shown, respectively, in Fig. 3 *C* and *D*. Note that we have not distinguished between the defect types of SFT and dislocation loops since they are too small to be identified with good precision. The lower bound of cluster size that can be detected from the TEM image is about 1.0 nm (in diameter). Defect clusters smaller than this size are not counted in the statistics of defect clusters characterized by in situ TEM.

As noted above, the average size of the defect clusters in 1,000 °C-aged (LCO) CrCoNi is smaller than that in the water-quenched (RSS) sample when the irradiation dose is relatively low. However, this difference becomes negligible when the irradiation dose is increased to ~0.6 dpa; instead, the number density of defect clusters is significantly smaller in 1,000 °C-aged (LCO) CrCoNi than that in the water-quenched (RSS) sample over the entire range of irradiation doses from 0.16 to 1.0 dpa. These results quantitatively indicate that the presence of LCO suppresses the formation of defect clusters, especially their number density, in irradiated CrCoNi alloys.

Primary Damage Simulations. To obtain further insight into the microscopic characteristics of the formation and evolution of defects in these alloys, we have performed primary damage simulations to investigate the initial stage of the irradiation

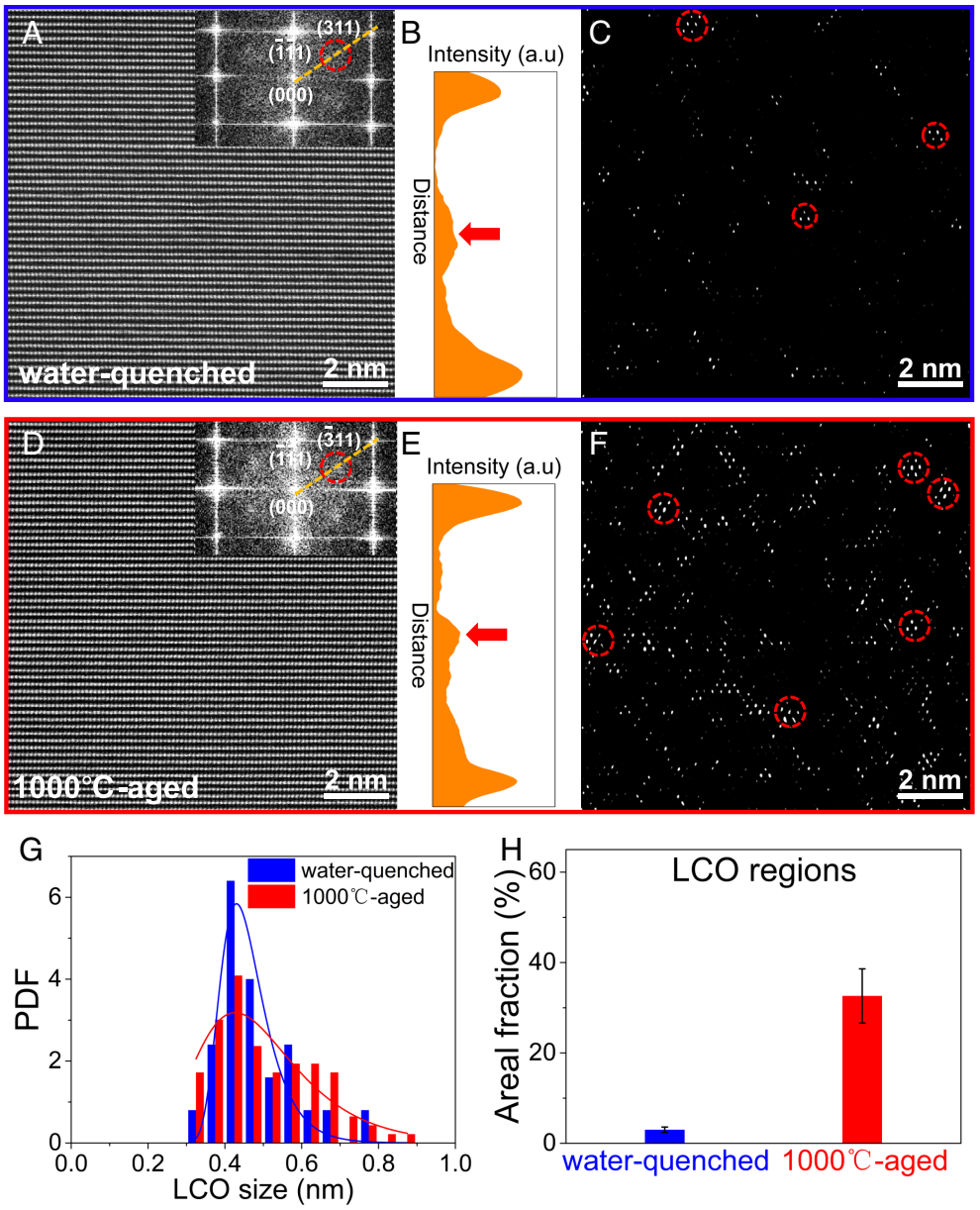

Fig. 1. Experimental characterization of LCO. (*A*) HAADF-STEM images of the water-quenched CrCoNi alloy in the [112] zone axis; the *Inset* shows the corresponding FFT, where the red circles indicate diffuse disks at 1/2{3_11} positions, suggesting the chemically short-range-ordered regions (CSROs) have sizes below one nanometer. (*B*) Diffraction intensity along the orange dashed line in panel (*A*). The red arrow indicates the extra intensity at 1/2{3_11} positions. (*C*) IFFT image based on four symmetrical diffraction disks, one of which is highlighted using a dashed circle in panel (*A*). Several CSRO regions are marked using red circles. (*D*–*F*) The same characterization as in the *Upper* panels for the 1,000 °C-aged sample. (*G*) Probability density function (PDF) of LCO size (in diameter). (*H*) Areal fraction of the LCO regions in the two CrCoNi alloys.

response of the RSS CrCoNi alloy and the one after annealing at 1,300 K (LCO CrCoNi). In addition to the MEAs, we have also considered pure Ni as a benchmark for comparison. Previous experimental studies (6, 30) have found that the CrCoNi alloy exhibits an improved irradiation tolerance compared to pure Ni, which has been attributed to its enhanced chemical complexity from an increasing number of principal elements.

First, we quantify the extent of LCO in the simulated CrCoNi alloys. Snapshots of the atomic configurations in the RSS and LCO CrCoNi alloys are shown, respectively, in Fig. 4 *A* and *B*. Fig. 4*C* gives a quantitative description using the Warren–Cowley order parameter for the first three nearest-neighbor shells of the LCO CrCoNi alloy. The Warren–Cowley parameters for the m^{th} nearest-neighbor shell is defined as (31):

$$\delta_{ij}^{m} = 1 - \frac{N_{ij}^{m}}{N^{m} \times X_j}, \qquad [1]$$

where N_{ij}^{m} denotes the number of j-type atoms in the m^{th} nearest-neighbor shell around an i-type atom, N^{m} is the total number of atoms in the m^{th} nearest-neighbor shell around an atom of interest, and X_j is the corresponding concentrations of type j in the alloy. For a random alloy, in the current case RSS, $\delta_{ij}^{m} = 0$. Positive values of δ_{ij}^{m} correspond to a tendency of unfavored i–j pairs; negative values pertain to favored pairs.

All δ_{ij}^{m} values deviate more or less from the ideal solid solution in either the positive or negative direction. For the first neighbor shell, we find a Warren–Cowley parameter of 0.2 for Cr–Cr,

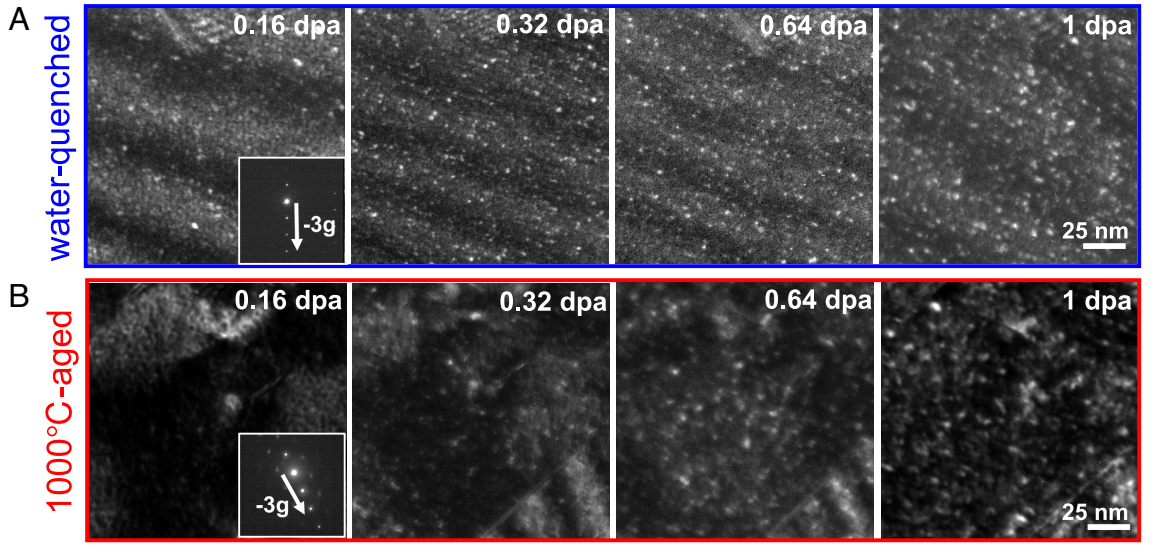

Fig. 2. TEM characterization of He^+ in situ irradiation. TEM images of (*A*) the water-quenched (RSS), and (*B*) the 1,000 °C-aged (LCO) CrCoNi alloys following various irradiation doses. The irradiation dose progressively increases from 0.16 dpa to 1.0 dpa from left to right.

indicating that this is a strongly unfavored pair. The pairs of Cr–Co and Ni–Ni, by contrast, have Warren–Cowley parameters of, respectively, −0.26 and −0.19, indicating a tendency toward small clusters of Cr–Co and Ni, which are also visible in Fig. 4*B*. Beyond the first coordination shell, the LCO is still present but become less pronounced.

MD simulations of irradiation damage were initiated by creating a primary-knock-on atom (PKA), which generates a cascade of particle collisions in the material. Further details of these irradiation simulations are given in *Methods*. The production and evolution of defects are of primary interest during such cascade simulations. First, to probe the evolution of defects during the cascade simulations, we monitored the number N_{FP} of pairs of interstitials and vacancies, i.e., Frenkel pairs (FPs), as a function of time for the RSS, LCO, and Ni at 5, 10, 20, and 40 keV. The

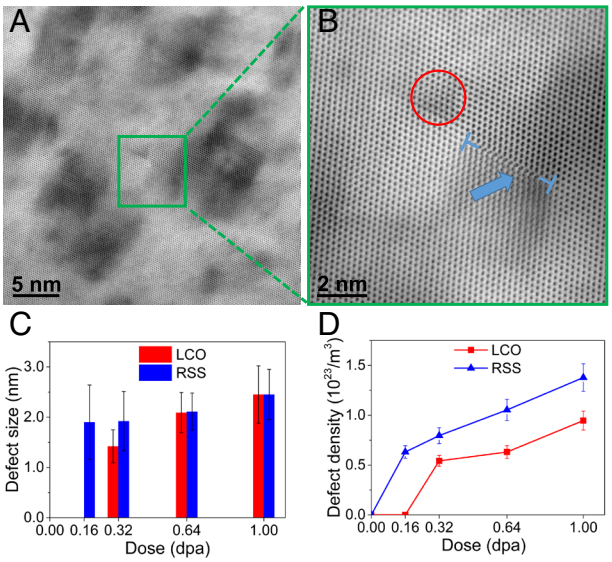

Fig. 3. Statistics of defect clusters after different irradiation doses. (*A*) STEM-BF image for the RSS CrCoNi after an irradiation dose of 1.0 dpa. (*B*) Enlarged image of the green box in (*A*) shows a stacking-fault tetrahedron and a <111> dislocation loop with the [110] zone axis marked with red circle and blue arrow, respectively. (*C*) Average size (in diameter) and (*D*) number density of defect clusters for the RSS and the LCO CrCoNi.

Wigner–Seitz cell method was used to identify the vacancy and interstitial point defects. This method works by taking the initial defect-free configuration as the reference for analyzing the presence of defects in the displaced configurations during the cascade displacement. As an example, Fig. 5*A* shows the results obtained from the cascade simulations using a Ni PKA energy of E_{PKA} = 40 keV. It is apparent that the number of FPs builds up very rapidly during the initial collision phase, reaching the so-called thermal spike (i.e., the maximum number of FPs) in about 1.0 ps. The peak N_{FP} value was found to be the largest for the CrCoNi alloys, with the value in the LCO CrCoNi being slightly lower than that in the RSS, and the smallest for the irradiated Ni. With increasing simulation time, most of the defects recombine during the relaxation of the thermal spike, leaving only a small number of surviving FPs at the end of the primary damage stage. However, the RSS and LCO CrCoNi samples were observed to exhibit the fewer surviving FPs relative to Ni, with the smallest number of FPs surviving in the LCO sample. Such a trend was found to be unaffected by the PKA energy, although the difference between the three materials became more pronounced with increasing E_{PKA} (Fig. 5*B*).

The more FPs at the peak and the fewer surviving pairs at the end of the cascades in CrCoNi alloys suggest that one of the key factors controlling FP reduction, especially in the LCO sample, is a higher efficiency in terms of defect recombination after the thermal spike. First, from Fig. 5*A*, the defect recombination rate can be calculated as $100 \times (N_{peak} - N_{end})/N_{peak}$, where N_{peak} and N_{end} are, respectively, the peak number and the surviving number of FPs. For the 40 keV PKA simulations, we find that the recombination rates in the RSS and the LCO CrCoNi are nearly the same, with a value of 99.6 ± 0.1%. This value is slightly higher than a value of 99.1 ± 0.2% for Ni. These high recombination rates are also compatible with the results of previously published simulations of primary damage in HEAs (8, 12). However, this result indicates that the recombination rate is not really a sensitive quantity to characterize the distinctive defect evolution in the three alloys. To better compare the defect evolution of the LCO and RSS alloys during the cascade simulation, we also plot in Fig. 5*A* the ratio between the number of FPs in the LCO and RSS. One observes that the difference in defect evolution starts to be seen in the late ballistic phase of the collision cascades, i.e. at ~1

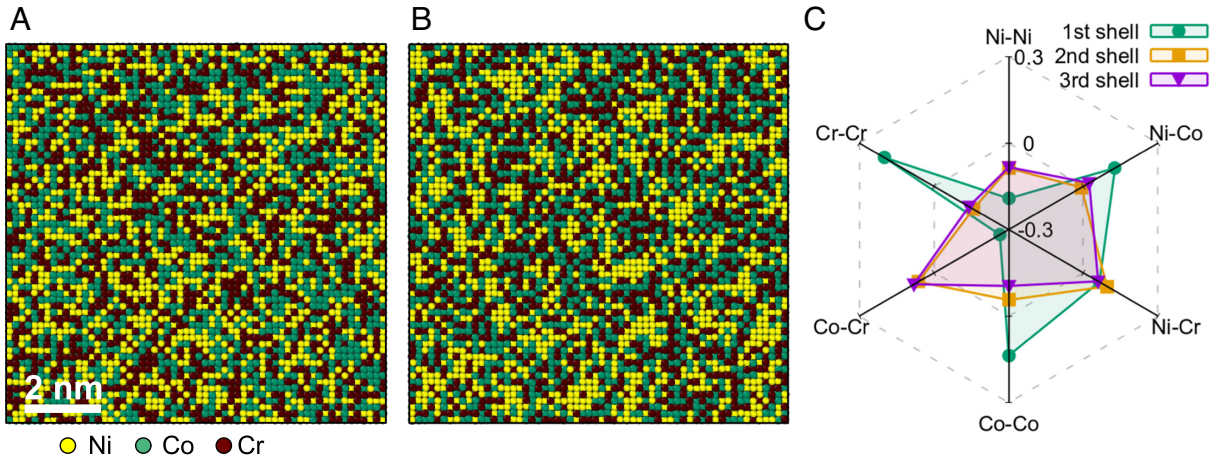

Fig. 4. Local structural analysis of the RSS and LCO CrCoNi alloys. (*A* and *B*) Representative configurations of the RSS and the LCO CrCoNi alloys, respectively. (*C*) Warren–Cowley parameters calculated for the first three nearest-neighbor shells of the LCO CrCoNi alloy.

ps., although up to the thermal spike, the difference between the two alloys is still small. This weakly suppressed generation of FPs in the LCO relative to that in the RSS can be attributed to the slightly larger FP formation energy in the LCO alloy, as we will see later. Thus, we conclude that the presence of LCO (at least to the degree of CSRO investigated in the current work) has only a minor effect on the irradiation-induced defect generation. Moreover, one sees that the different behavior between the LCO and RSS alloys becomes progressively more pronounced during the cooling phase, i.e., in the region where the kinetics play a critical role in affecting defect recombination and annihilation. Finally, we note that the ratio between the LCO and RSS as plotted in Fig. 5*A* is a better (more sensitive) indicator of the different behavior of the two CrCoNi alloys during the cascade recovery.

Further insight into the primary irradiation damage can be achieved by analyzing the resulting defect clusters at the end of the cascade simulations. Several types of defect clusters, such as SFT and dislocation loops, were identified by combining the dislocation extraction method (32) and polyhedra template matching method (33) with a root-mean-square deviation cutoff parameter chosen to be 0.2. Corresponding representative distributions of defect sites and dislocations at the final stage of the primary damage for the RSS and LCO CrCoNi alloys and pure Ni are given in Fig. 6*A*, which indicates that the resulting states of primary damage in the three samples are quite different. For pure Ni, both interstitials and vacancies tend to accumulate and form clusters, e.g., via the formation of 1/3<111> faulted dislocation loops and SFTs comprised of a set of 1/6<110> dislocations. These results agree well with previous simulations and experiments on the irradiation damage of Ni and Ni-based alloys (7, 8, 30, 34–36). For the RSS CrCoNi alloy, these defect clusters are still present, but their size and number density are reduced compared to that in pure Ni. Among all three samples, the LCO CrCoNi alloy was found to contain the smallest and least defect clusters, which is consistent with the trend for these materials of retaining the fewest surviving FPs at the end of the primary damage stage (Fig. 5*B*).

In terms of a quantitative analysis of the irradiation-induced defect clusters, which consist of vacancies and/or interstitials, their size and number were determined by using the second nearest-neighbor distance as the cutoff. First, we present in Fig. 6*B* the accumulative probability of clusters, i.e., the probability to find clusters with size smaller than or equal to a given cluster size, N_{cluster}. It is clear that the chance to find a defect cluster of a given size is not the same in the three alloys. For the convenience of discussion, here we divide the cluster size into three ranges, namely small ($N_{\text{cluster}} < 8$), intermediate ($8 \le N_{\text{cluster}} \le 30$), and large clusters ($N_{cluster} > 30$). The influence of LCO is seen in that the LCO alloy contains basically no large clusters after PKA, whereas the probability of finding small-sized ($N_{\text{cluster}} \le 7$) clusters is higher than that in the RSS and pure Ni. This result indicates that the presence of LCO suppresses the emergence of large

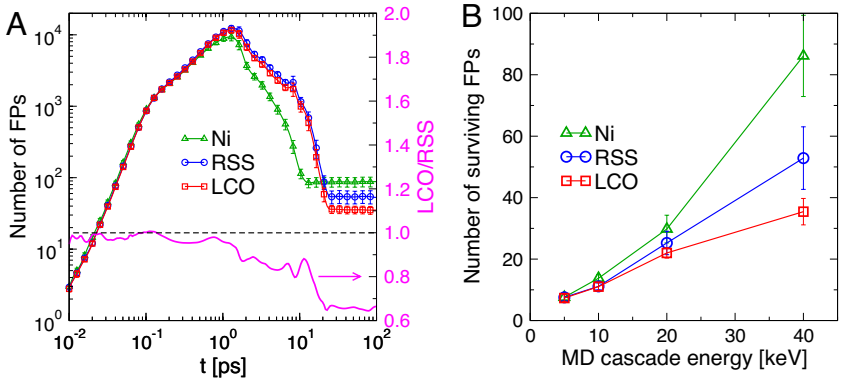

Fig. 5. The evolution of FPs. (*A*) Number of FPs N_{FP} as a function of simulation time for all cascade simulations with 40 keV PKA energy. The solid magenta line represents the ratio between the number of FPs in the LCO and RSS alloys, see the right ordinate. (*B*) Number of surviving FPs at different PKA energies.

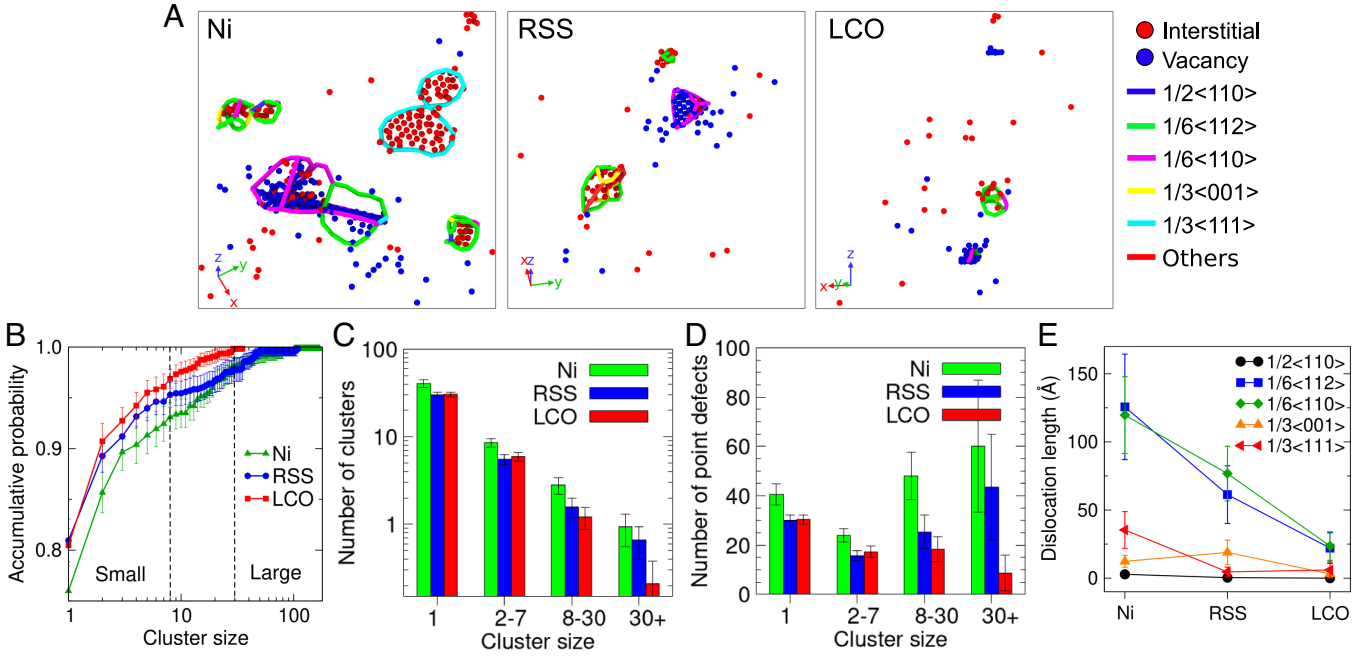

Fig. 6. Comparison of the defect clusters resulted from cascade simulations with 40 keV PKA energy. (*A*) Defect morphology. Spheres in red and blue represent interstitial and vacancy sites, respectively. Lines of different colors correspond to dislocations of different types as labeled on the right. (*B*) Accumulative probability of defect clusters. (*C*) Distribution of defect clusters of different sizes. (*D*) Number of point defects in clusters of four different size ranges. (*E*) Average lengths of the dislocation lines of various types. The mean and the SEM (error bar) were obtained from 15 to 25 independent PKA with E_{PKA} = 40 keV.

clusters, which can be attributed to defect kinetics rather than thermodynamics as we will see later.

Fig. 6*C* shows in a more quantitative manner the number of defect clusters in various size ranges. First, one sees that the two MEAs after irradiation contain less defect clusters than pure Ni in the entire distribution spectrum, indicating that increasing chemical complexity does help to delay defect clustering (22, 23). Moreover, one observes that although the LCO and RSS alloys contain a similar number of defect clusters, the LCO effect is manifested in the reduced number of intermediate- and large-sized clusters. Most notably, the number of point defects contained in the large-sized clusters of the LCO structure after each PKA is much less than that in the RSS structure (Fig. 6*D*), and this difference amounts to ~35% of the surviving FPs in the RSS. On average, a large-sized cluster in the irradiated RSS and LCO structures contains, respectively, 65 and 42 point defects, comparable to the lower bound of the cluster size observable from the TEM experiments.

Importantly, we note that only the large-sized clusters (and potentially the intermediate-sized ones) should be counted for a fair and meaningful comparison of the defect densities in the experimental and MD-simulated samples. This is because the small-sized clusters, if present, are not only undetectable by in-situ TEM (due to the limitation in resolution), but also susceptible to dissolution and annihilation during evolution of the irradiation-induced defects over experimental timescales. In contrast, the large-sized clusters as shown in Fig. 6*C* are prone to growth with time and eventually be detected in experimental characterization. Fig. 6 clearly shows that there is a significant difference in the number density of large-sized clusters in the two MEAs after irradiation, in accordance with the TEM results (Fig. 3). Thus, we conclude that the presence of LCO strongly affects the defect clustering behavior.

Another useful parameter for describing the defect clusters is the lengths of various types of dislocations at the end of the cascade simulations. Fig. 6*E* shows that the two major types of dislocations are the 1/6<112> and 1/6<110>; their average lengths can be seen to progressively decrease when comparing Ni to RSS CrCoNi and LCO CrCoNi. In fact, all the results in Fig. 6 indicate that the lowest degree of primary irradiation damage is found in the LCO CrCoNi alloy, as compared to the RSS and pure Ni samples, implying that the presence of LCO can enhance the resistance to irradiation damage.

Finally, it is worth noting that the irradiation not only generated defects in these materials, but also resulted in a change in the local chemical ordering, particularly for the region near the cascade core. In *SI Appendix*, Fig. S2*A*, we show that a certain degree of LCO develops during PKA in the RSS, which can be attributed to the fact that the thermally activated local atomic arrangements always tend toward a lower free-energy state, i.e., atomic configurations with a higher degree of CSRO (see, e.g., ref. 37). Correspondingly, the LCO would not be much decreased during PKA either (*SI Appendix*, Fig. S2*B*). The much higher degree of chemical order retained in the LCO CrCoNi alloy is expected to also influence the evolution of defects after the primary damage state (corresponding to the experimental results presented in this work). In *SI Appendix*, Fig. S2 *C* and *D*, we show that the degree of LCO first increases and then converges with increasing PKA energy, consistent with previous simulation and experimental findings (37, 38). The convergence of the degree of LCO with increasing irradiation dose has been attributed to the balance between two competing effects induced by irradiation, namely, the thermal activation for chemical ordering versus the rerandomization of the constituent elemental distribution (38).

Energetics of FPs and Defect Clustering by MD Simulation. Both the irradiation experiments (for the CrCoNi) and primary damage simulations have demonstrated the enhanced resistance to irradiation damage of the LCO CrCoNi alloy as compared to the RSS CrCoNi and pure Ni. A salient question that immediately arises is how the presence of local chemical ordering can diminish the irradiation damage in this multi-principal element alloy? To answer this

question, we first probe the effect of LCO on the thermodynamics of the defects, i.e., the formation energies of FPs and binding energy of defect clustering, which are both performed randomly in the supercell for the three samples.

First, the formation energies of FPs are expected to influence the build-up of defects and their numbers at the thermal spike. In practice, we have calculated the formation energy of a FP using the expression: $E_f = E_{vac} + E_{int} - 2E_0$, where E_0, E_{vac}, and E_{int} are, respectively, the energies of the original sample, the original sample containing a single randomly created vacancy or interstitial. The formation energies of about 10,000 FPs were calculated for both the RSS and LCO CrCoNi alloys. Based on our simulations, a comparison of the distribution of the formation energies of FPs in the three investigated alloys is shown in Fig. 7*A*. The formation energy of FPs for pure Ni (indicated by the dashed line) is 5.87 eV, which is considerably larger than the formation energies of the FPs in the two CrCoNi structures. The RSS CrCoNi exhibits a broad distribution of the formation energies with a mean value of 4.29 eV. By contrast, the distribution for the LCO CrCoNi is significantly narrower with an average value of 4.39 eV. This difference in formation energies of the FPs in the three samples can be used to rationalize the observations in Fig. 5*A* regarding the number of FPs at the thermal spike. While the difference between the RSS and LCO is small in terms of irradiation-induced defect generation, it is obvious from the number of FPs in LCO and RSS alloys in Fig. 5*A* that the presence of LCO facilitates the annihilation of defects during the cooling phase of the collision cascade; as will become evident later, this is mainly due to the LCO-mediated changes in the defect kinetics.

Second, the binding energies of interstitial or vacancy clusters (e.g., dislocation loops, SFT, shown by the simulations in Fig. 6*A*) can be used to evaluate the energetic preference for defect clustering. The total binding energy of a defect cluster with n interstitials or vacancies can be obtained directly from its formation energy, which is defined as the energy difference between a configuration in which the defects (interstitials or vacancies) can interact with each other and one where all the defects are sufficiently well separated that no such interactions are possible. The total binding energy of a defect cluster containing n interstitials or vacancies can thus be defined as (39):

$$E_b^{d_1,d_2,\ldots,d_n} = \sum_{i=1}^{n} E_f^{d_i} - E_f^{d_1,d_2,\ldots,d_n}, \qquad [2]$$

where $E_f^{d_i}$ denotes the formation energy of the ith system containing a single interstitial or vacancy point defect d_i and $E_f^{d_1,d_2,\ldots,d_n}$ is the formation energy of a defect cluster with n interacting interstitials or vacancies.

For the RSS and LCO CrCoNi alloy structures, as well as the pure Ni, we consider here two characteristic defect clusters, specifically the 1/3<111> faulted dislocation loops and SFT (Fig. 3*A*); their simulated binding energies, E_b, as a function of size are shown, respectively, in Fig. 7 *B* and *C*. For both 1/3<111> faulted dislocation loops and SFT, the total binding energy progressively increases with increasing cluster size (in terms of the number of point defects the cluster is comprised of) for all three alloys. It is interesting to note that the binding energy of the 1/3<111> dislocation loops and SFT is larger in pure Ni than that in the RSS and LCO CrCoNi, suggesting that such type of defect clusters is thermodynamically more favored in pure Ni than that in CrCoNi alloy. It is also important to note that the RSS and LCO CrCoNi have almost the same binding energy of the 1/3<111> dislocation loops and SFT, implying that the presence of LCO does not noticeably change the thermodynamic stability of the defect clusters.

Mobility of Vacancies and Interstitials by MD Simulation. The CrCoNi alloy, in both the RSS and LCO conditions, exhibit almost the same binding energy of defect clustering (Fig. 7 *B* and *C*). This seems to be in contradiction with the statistical analysis of the defect clusters depicted in Fig. 6*C*, which shows that although the RSS and LCO CrCoNi contain a similar volume fraction of small defect clusters (with size less than 10 atoms), damage in the LCO alloy displays less large-sized clusters. Therefore, it is essential to also examine the mobility of the vacancies and interstitials, as their kinetics should significantly influence the defect recombination as well as the surviving defect clusters. Specifically, the closer the diffusivities are of the vacancies and interstitials, the higher the chance of defect annihilation because of the recombination between these two types of point defects.

We have performed MD simulations at various temperatures for the defect-containing (irradiation damaged) samples to investigate the mobility of the vacancies and interstitials; details of the procedures used are described in the *Methods*. Fig. 8*A* shows the mean square displacements (MSDs), $<R^2>$, for interstitials and vacancies in the RSS and LCO CrCoNi at 1,200 K, where it is apparent that the LCO alloy exhibits much slower diffusion for both types of point defects, consistent with the finding of recent

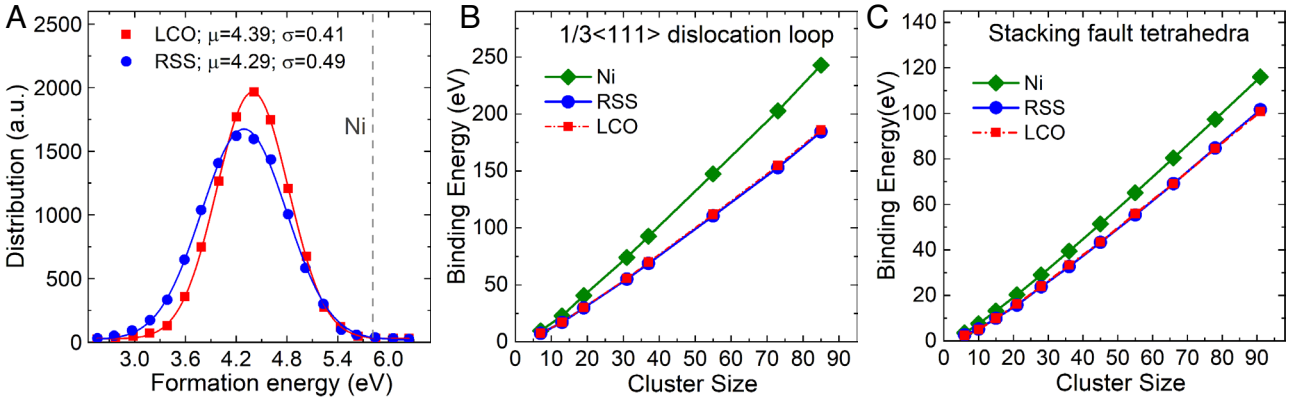

Fig. 7. Formation energies of FPs and binding energy of defect clustering. (*A*) The distribution of formation energies of FPs in the RSS and LCO CrCoNi alloys. The dashed line indicates the formation energy of FPs for pure Ni. The solid lines are Gaussian fits to the RSS and LCO data. μ and σ represent, respectively, the mean value and SD of the distribution profiles. (*B*) Binding energy of 1/3<111> faulted dislocation loops and (*C*) binding energy of SFTs for the RSS and LCO CrCoNi alloys, both compared with pure Ni. The binding energies for the RSS and LCO CrCoNi alloys are derived from the statistical average of 10 independent samples for each type of defect clusters.

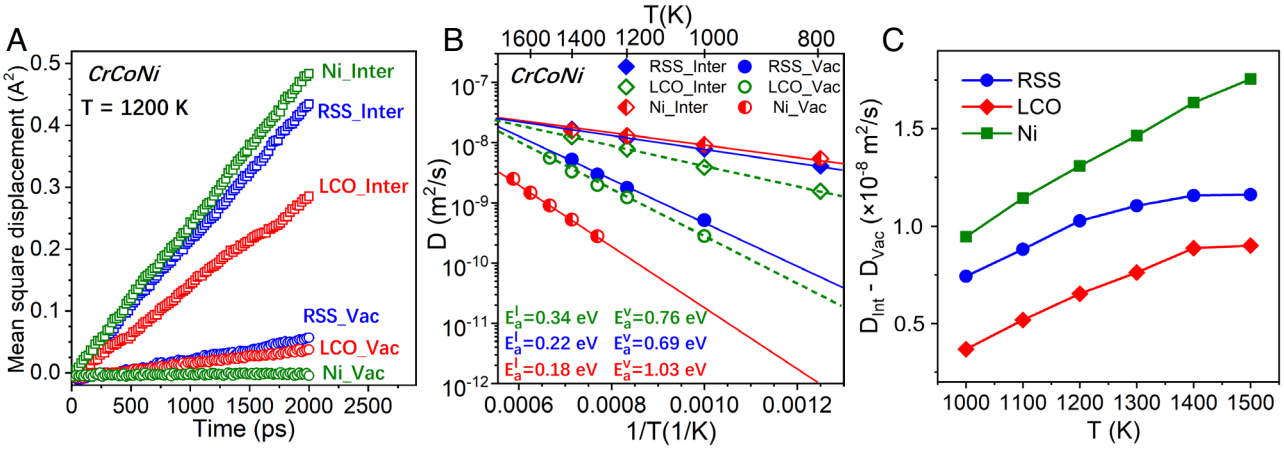

Fig. 8. Diffusion of point defects in pure Ni and in the RSS and LCO CrCoNi samples. (*A*) Mean square displacement (MSD) for vacancies and interstitials at 1,200 K. (*B*) The tracer diffusion coefficient (*D*) for vacancies and interstitials at various temperatures. (*C*) The difference between the interstitial diffusion coefficient (D_{int}) and vacancy diffusion coefficient (D_{vac}) at various temperatures.

simulation studies (40, 41). The diffusivities of the point defects at various temperatures are plotted in Fig. 8*B*, from which the activation energy (E_a) for diffusion of the point defects can be calculated: for the RSS CrCoNi, the E_a for interstitials and vacancies are 0.22 eV and 0.69 eV, respectively, whereas for the LCO CrCoNi, E_a for the interstitial diffusion is 0.34 eV and 0.76 eV for vacancy diffusion. Such findings demonstrate the role of LCO in slowing down the mobility of both vacancies and interstitials. Interestingly, the difference in activation E_a energies for interstitial and vacancy diffusion is 0.47 eV and 0.42 eV, respectively, for RSS and LCO samples, implying the more pronounced reduction in interstitial mobility due to the presence of chemical order. In contrast, the difference of E_a between interstitial and vacancy for pure Ni is about 0.85 eV, which is much larger than that for either of the two CrCoNi conditions. Fig. 8*C* shows that the LCO sample also has a smaller difference between the mobility of vacancies and interstitials when compared to that in the RSS sample.

To further understand why LCO has a stronger effect on the mobility of interstitials than vacancies, we have calculated for the RSS and LCO CrCoNi alloys the correlation factor, f (42), which is defined as $f = \langle R^2\rangle/\langle R_{random}{}^2\rangle$, where $\langle R^2\rangle$ is MSD and $\langle R_{random}{}^2\rangle$ is a hypothetical MSD arising from uncorrelated jump sequences (or uncorrelated random walk). Here, $\langle R_{random}{}^2\rangle = n^*\lambda^2$, where n is the number of jumps and λ is the jump length for each jump of the defects (λ = 2.5 Å). The value of $f < 1$ indicates the nonrandom nature of diffusion that reduces the efficiency of atomic jumps in the presence of positional memory effects with respect to an uncorrelated random walk. Using MD simulations, we calculated the correlation factor for the diffusion of tracer atoms of vacancy/interstitial-containing RSS and LCO CrCoNi alloys at 1,200 K. The corresponding $\langle R^2\rangle$ and $\langle R_{random}{}^2\rangle$ as a function of time are shown in *SI Appendix*, Fig. S3. We find that the correlation factor for interstitials is reduced from 0.232 ± 0.007 for RSS to 0.165 ± 0.009 for LCO, i.e., by 29%. In contrast, the correlation factor for vacancies is decreased from 0.50 ± 0.01 for RSS to 0.44 ± 0.02 for LCO, i.e., by 12%. These results demonstrate that LCO can considerably localize the diffusion of point defects, originating from the reduced efficiency of atomic jumps (i.e., smaller f). The stronger effect of LCO in localizing the motion of interstitials is in line with the finding that the activation energy (i.e., migration barrier) for interstitials is increased to a larger extent than for vacancies when LCO is introduced (Fig. 8). This LCO-induced localization of the motion of point defects and the reduced mobility difference between interstitials and vacancies promote the recombination/annihilation of irradiation-generated defects, which explains the better irradiation tolerance of the LCO CrCoNi over RSS CrCoNi and pure Ni.

These differences in the energetics and diffusivities of point defects suggest a two-pronged effect of LCO on resistance to irradiation damage: i) The presence of LCO tends to slow down the diffusion of both the interstitials and vacancies, thus localizing the migration of those two types of point defects; and ii) the LCO narrows the difference in mobility between interstitials and vacancies (interstitials generally diffuse much faster than vacancies), thus giving them a higher probability of recombination and thus annihilation in the collision cascade. These two effects both result in less surviving defects in the LCO CrCoNi alloy after irradiation, which explains our experimental results shown in Figs. 2 and 3. For example, we found difficulty in detecting defect formation in the LCO CrCoNi structure at a low irradiation dose of 0.16 dpa, which is certainly consistent with the more effective recombination of defects in the presence of LCO, giving rise to a lower residual defect concentration and less larger scale observable defect clusters. As the irradiation dose is increased, some small defect clusters start to appear in the LCO alloy, but their number density and size are still smaller than in the RSS CrCoNi. As the irradiation dose is gradually increased to 1.0 dpa, the defect sizes in both the LCO and RSS cases approach saturation with a slow increase in the defect number density; however, this density is always smaller in the LCO sample. This indicates that although irradiation damage in the form of defect clusters can still be generated in the LCO sample at high irradiation doses, on a larger time scale the reduced point defect mobility in the presence of LCO inhibits the growth of such clusters.

Conclusions

To conclude, both the ion irradiation experiments and the primary damage simulations demonstrate that the presence of LCO in the CrCoNi MEA can effectively improve its resistance to irradiation damage at relatively low irradiation doses. This improvement is not only manifested as a reduced number of surviving point defects and large-sized defect clusters after the primary damage phase, but also by the suppressed generation of defect clusters as the irradiation dose is increased. We rationalize the different resistance to irradiation damage exhibited by the three alloys (the RSS CrCoNi alloy, CrCoNi with

considerable LCO in the form of CSRO, and pure Ni) by tracking the differences in the energetics and kinetics of their damage-induced point defects and their clustering. Although the binding energies of defect clustering for the RSS and LCO CrCoNi are very similar, the effect of LCO is clearly seen in the mobility of interstitials and vacancies: LCO increases the energy barriers for defect diffusion, lowering the mobility of the two types of point defects. Consequently, the slower diffusion of the vacancies and interstitials, in particular the reduced difference in their mobility, renders these defects more likely to recombine, thus resulting in less surviving damage after irradiation. This observation resonates with the LCO-roughened energy landscape that changes dislocation activities (18) to influence mechanical properties such as strength and strain hardening (43, 44), as well as the 3-D migration behavior of point defects (45) discovered recently in MEAs. Tailoring the composition and heat-treatment of H/MEAs is expected to change the degree and extent of LCO, which can be extended beyond CSRO into medium (<~2 nm) range or even long range in one or two dimensions of the LCO domain. Another way to boost LCO is to add interstitial alloying elements (such as C, N) that have chemical affinity preferentially with some of the constituent principal elements (41). The tunability of LCO thus provides a means to enhance irradiation tolerance, such that multiprincipal element solid solution alloys (without precipitates) may offer an interesting alternative to traditional alloys for demanding nuclear environments.

Methods

Experimental Procedures. The preparation of water-quenched and 1,000 °C-aged CrCoNi samples followed the procedure reported in ref. 14. First, the raw ingot of CrCoNi alloy was argon-arc melted and then cut into smaller samples. These samples were all homogenized at 1,200 °C for 48 h, then underwent two different thermal treatments: i) water quenched to room temperature (denoted as water-quenched); ii) aged at 1,000 °C for 120 h followed by furnace cooling (denoted as 1,000 °C-aged).

Atomic-scale characterization of LCO was performed using the Cs-corrected TEM under a high-angle annular dark field (HAADF) mode in Thermo Fisher Themis Z equipment operated at 300 keV. TEM samples were prepared by the twin-jet electropolishing using 5 vol% perchloric acid and 95 vol% ethanol at −30 °C. The HAADF atomic images for water-quenched and 1,000 °C-aged CrCoNi were obtained under [112] zone axis, and the diffraction disks corresponding to LCO were detected at the position of 1/2{3_11} by using the fast Fourier transform (FFT). The inversed FFT (IFFT) of the images based on this diffraction information can further reveal the size and distribution of the LCO. The size and area fraction of LCO regions for water-quenched and 1,000 °C-aged CrCoNi were then obtained from multiple IFFT images acquired with the same settings for contrast and brightness. The total examined region covered an area of approximately 500 nm^2 to achieve adequate statistics.

Ion irradiation of the water-quenched and 1,000 °C-aged CrCoNi samples were performed at the Xiamen Multiple Ion Beam In-situ TEM Analysis Facility. TEM samples were prepared using twin-jet electropolishing for in situ experimental observation; irradiation was carried out at 300 K using 50 keV He ions. The in situ TEM observations were performed using a TECNAI G20 F30 microscope with a field emission gun operating at 300 kV. The images were taken using a (g, -3g) weak-beam dark-field (WBDF) condition with $g = (200)$ by pausing the ion beam at various doses.

MD-Simulated Alloy Preparation. MD simulations were carried out to prepare the model alloys using Large-scale Atomic/Molecular Massively Parallel Simulator software (LAMMPS) (46). Three model alloys–the RSS and LCO CrCoNi as well as pure Ni–were studied by adopting an empirical embedded atom method (EAM) potential for the CrCoNi system (18). It is worth noting that in the development of this potential, special attention has been paid to the accurate description of the energetics of various types of defects and transition pathways, which makes this interatomic potential suitable for primary damage simulations.

Cubic simulation boxes with an *fcc* structure were set up with a range of different sizes L as a function of the lattice parameter a_0, specifically, $L = 35a_0$, $50a_0$, $65a_0$, and $80a_0$, which correspond to 171,500, 500,000, 1,098,500, and 2,048,000 atoms, respectively. Periodic boundary conditions were applied in all directions. The RSS CrCoNi structures were initiated by randomly distributing equiatomic Ni, Co, Cr atoms into an *fcc* lattice with lattice parameter $a_0 = 0.352$ nm; this was subsequently relaxed at 300 K for 0.2 ns using a time-step of 2.0 fs and isothermal-isobaric ensemble under zero pressure. The corresponding LCO CrCoNi structures were prepared using the hybrid molecular dynamics/Monte Carlo (MD/MC) simulation scheme under the variance-constrained semigrand canonical ensemble (as already implemented in ref. 47). The variance constraint parameter $k = 1{,}000$ was used, in accordance with the settings of previous studies (18). The MD/MC simulations were performed at the target temperature of 1,300 K for 1,000,000 steps, which has been confirmed to achieve the converged potential energy and local chemical structure. Finally, the sample was quenched to 300 K and relaxed for 0.2 ns for the usage of the subsequent irradiation simulation.

MD-Simulated Irradiation. The MD-simulated irradiation process was induced in the model alloys by introducing a PKA with a sufficiently high kinetic energy which resulted in a collision cascade. For the PKA simulations, the EAM potential was smoothly joined to the universal repulsive Ziegler–Biersack–Littmark potential for small interatomic separations. PKA energies of 5, 10, 20, and 40 eV were modeled for the RSS and LCO CrCoNi, as well as pure Ni, using cubic simulation boxes containing 171,500, 500,000, 1,098,500, and 2,048,000 atoms, respectively. For each simulation, we first randomly selected a Ni atom in the box and then translated the box such that the selected Ni atom was positioned at [1/2L, 1/3L, 1/4L] with the origin of the box at [0, 0, 0], and L is the side length of the box. We have found that this choice of the PKA location can make better use of the simulation box than PKA at the box center for the chosen recoil direction [135]. The borders of the simulation box, with a thickness of 0.6 nm (four atomic layers), were coupled to a thermostat using the canonical ensemble such that the boundary layers were maintained at 300 K, imitating the energy dissipation into the bulk during irradiation. The interior of the simulation box, which encompasses the displacement cascade process, was simulated under the microcanonical ensemble. The electronic stopping effect was taken into account by implementing a friction force, using damping parameter $\gamma = 0.005$ eV /ps $Å^2$ to the atoms with kinetic energy lower than 10 eV (12). Adaptive time steps (ranging from 0.0001 to 2.0 fs) were used to allow for small steps in the early stage of atomic collision and a relatively large value as the energy exchange between the atoms decreases. The maximum distance for an atom to move in one timestep was chosen to be 0.01 nm, and the maximum energy change for an atom in one timestep was set to be 0.025 E_{PKA}. For statistical purposes, we have performed 15 to 25 cascades for each case to ensure the convergence of the final results. The error bar is estimated as the SEM of the tens of independent cascade simulations.

Diffusion of Vacancies and Interstitials. We performed MD simulations at various temperatures for the defects-containing samples to investigate the mobility of vacancies and interstitials. The initial atomic configurations consisted of 32,000 atoms, while a single interstitial dumbbell or vacancy atom was then introduced randomly into lattice sites. At each simulation temperature, the defect structure was first equilibrated over 5 ps under the isothermal-isobaric ensemble under zero pressure with a timestep of 1.0 fs prior to the diffusion data being collected from the subsequent 2.0 ns. The tracer diffusion coefficient (D), mean square displacement (MSD), $<R^2>$, for the RSS and LCO CrCoNi samples were obtained by averaging over three independent configurations and five different initial sites for interstitial and vacancy. The diffusion coefficient (D) can be calculated from the MSD at long time using the Einstein relation: $D = \mathrm{MSD}/(2nt)$, where t is time and n is equal to 3 here for describing the 3-D motions of interstitial atom and vacancy.

Data, Materials, and Software Availability. The data discussed in the paper and an example code for performing the primary damage simulation have been deposited in Zenodo (https://doi.org/10.5281/zenodo.7752605).

ACKNOWLEDGMENTS. We acknowledge the valuable discussion with Mark Asta and Shijun Zhao. Z.Z., J.D., and E.M. are indebted to Xi'an Jiaotong University for hosting their work at the Center for Alloy Innovation and Design. Z.Z., C.L., and

E.M. acknowledge National Natural Science Foundation of China (Grant No. 52231001). J.D. was supported by the Natural Science Foundation of China (Grant No. 12004294), National Youth Talents Program and the HPC platform of Xi'an Jiaotong University. This work is partially supported by the National Key Research and Development Program of China under Grant No.2019YFA0209900; the National Natural Science Foundation of China under Grant No. 12075179. R.O.R. was funded by the U.S. Department of Energy, Office of Science, Office of Basic Energy Sciences, Materials Sciences and Engineering Division, under contract no. DE-AC02-05-CH11231. In addition, we thank the Instrument Analysis Center of Xi'an Jiaotong University and the Xiamen Multiple Ion Beam In-situ TEM Analysis Facility.

Author affiliations: [a]Center for Alloy Innovation and Design, State Key Laboratory for Mechanical Behavior of Materials, Xi'an Jiaotong University, Xi'an 710049, China; [b]School of Nuclear Science and Technology, Xi'an Jiaotong University, Xi'an 710049, China; [c]Materials Sciences Division, Lawrence Berkeley National Laboratory, Berkeley, CA 94720; and [d]Department of Materials Science and Engineering, University of California, Berkeley, CA 94720

1. B. Gludovatz *et al.*, A fracture-resistant high-entropy alloy for cryogenic applications. *Science* **345**, 1153–1158 (2014).
2. B. Gludovatz *et al.*, Exceptional damage-tolerance of a medium-entropy alloy CrCoNi at cryogenic temperatures. *Nat. Commun.* **7**, 1–8 (2016).
3. Y. Shi, B. Yang, P. K. Liaw, Corrosion-resistant high-entropy alloys: A review. *Metals* **7**, 43 (2017).
4. Y. Shi *et al.*, Homogenization of $Al_xCoCrFeNi$ high-entropy alloys with improved corrosion resistance. *Corrosion Sci.* **133**, 120–131 (2018).
5. C. Lu *et al.*, Enhancing radiation tolerance by controlling defect mobility and migration pathways in multicomponent single-phase alloys. *Nat. Commun.* **7**, 1–8 (2016).
6. F. Granberg *et al.*, Mechanism of radiation damage reduction in equiatomic multicomponent single phase alloys. *Phys. Rev. Lett.* **116**, 135504 (2016).
7. C. Lu *et al.*, Radiation-induced segregation on defect clusters in single-phase concentrated solid-solution alloys. *Acta Mater.* **127**, 98–107 (2017).
8. Y. Lin *et al.*, Enhanced radiation tolerance of the Ni-Co-Cr-Fe high-entropy alloy as revealed from primary damage. *Acta Mater.* **196**, 133–143 (2020).
9. Y. Zhang, T. Egami, W. J. Weber, Dissipation of radiation energy in concentrated solid-solution alloys: Unique defect properties and microstructural evolution. *MRS Bull.* **44**, 798–811 (2019).
10. H.-S. Do, B.-J. Lee, Origin of radiation resistance in multi-principal element alloys. *Sci. Rep.* **8**, 1–9 (2018).
11. Y. Li, R. Li, Q. Peng, S. Ogata, Reduction of dislocation, mean free path, and migration barriers using high entropy alloy: Insights from the atomistic study of irradiation damage of CoNiCrFeMn. *Nanotechnol.* **31**, 425701 (2020).
12. O. R. Deluigi *et al.*, Simulations of primary damage in a high entropy alloy: Probing enhanced radiation resistance. *Acta Materialia.* **213**, 116951 (2021).
13. Y. Zhang, Y. N. Osetsky, W. J. Weber, Tunable chemical disorder in concentrated alloys: Defect physics and radiation performance. *Chem. Rev.* **122**, 789–829 (2022).
14. R. Zhang *et al.*, Short-range order and its impact on the CrCoNi medium-entropy alloy. *Nature* **581**, 283–287 (2020).
15. X. Chen *et al.*, Direct observation of chemical short-range order in a medium-entropy alloy. *Nature* **592**, 712–716 (2021).
16. L. Zhou *et al.*, Atomic-scale evidence of chemical short-range order in CrCoNi medium-entropy alloy. *Acta Mater.* **224**, 117490 (2022).
17. J. Ding, Q. Yu, M. Asta, R. O. Ritchie, Tunable stacking fault energies by tailoring local chemical order in CrCoNi medium-entropy alloys. *Proc. Natl. Acad. Sci. U.S.A.* **115**, 8919–8924 (2018).
18. Q.-J. Li, H. Sheng, E. Ma, Strengthening in multi-principal element alloys with local-chemical-order roughened dislocation pathways. *Nat. Commun.* **10**, 3563 (2019).
19. S. Yin *et al.*, Atomistic simulations of dislocation mobility in refractory high-entropy alloys and the effect of chemical short-range order. *Nat. Commun.* **12**, 1–14 (2021).
20. B. Zhang, J. Ding, E. Ma, Chemical short-range order in body-centered-cubic TiZrHfNb high-entropy alloys. *Appl. Phys. Lett.* **119**, 201908 (2021).
21. Y. Bu *et al.*, Local chemical fluctuation mediated ductility in body-centered-cubic high-entropy alloys. *Mater. Today* **46**, 28–34 (2021).
22. L. Q. Liu *et al.*, Local chemical ordering and its impact on radiation damage behavior of multi-principal element alloys. *J. Mater. Sci. Tech.* **135**, 13–25 (2023).
23. Y. Li *et al.*, Chemical ordering effect on the radiation resistance of a CoNiCrFeMn high-entropy alloy. *Comp. Mater. Sci.* **214**, 111764 (2022).
24. T. Shi *et al.*, Unconventional energetics of small vacancy clusters in BCC high-entropy alloy Nb0.75ZrTiV0.5. J. *Mater. Sci. Technol*. **146**, 61–71 (2023).
25. Z. Wu, Y. Gao, H. Bei, Thermal activation mechanisms and Labusch-type strengthening analysis for a family of high-entropy and equiatomic solid-solution alloys. *Acta Mater.* **120**, 108–119 (2016).
26. Y. Zhang *et al.*, Influence of chemical disorder on energy dissipation and defect evolution in advanced alloys. *J. Mater. Res.* **31**, 2363–2375 (2016).
27. J. F. Ziegler, J. P. Biersack, M. D. Ziegler, *SRIM - the Stopping and Range of Ions in Matter* (SRIM Co., Chester, Maryland, USA, 2008).
28. H. Zhu *et al.*, The formation and accumulation of radiation-induced defects and the role of lamellar interfaces in radiation damage of titanium aluminum alloy irradiated with Kr-ions at room temperature. *Acta Mater.* **195**, 654–667 (2020).
29. Y.-R. Lin, W.-Y. Chen, M. Li, J. Henry, S. J. Zinkle, Dynamic observation of dual-beam irradiated Fe and Fe-10Cr alloys at 435° C. *Acta Mater.* **209**, 116793 (2021).
30. Y. Zhang *et al.*, Influence of chemical disorder on energy dissipation and defect evolution in concentrated solid solution alloys. *Nat. Commun.* **6**, 1–9 (2015).
31. J. M. Cowley, An approximate theory of order in alloys. *Phys. Rev.* **77**, 669 (1950).
32. A. Stukowski, V. V. Bulatov, A. Arsenlis, Automated identification and indexing of dislocations in crystal interfaces. *Model. Simul. Mater. Sci. Eng.* **20**, 085007 (2012).
33. P. M. Larsen, S. Schmidt, J. Schiøtz, Robust structural identification via polyhedral template matching. *Model. Simul. Mater. Sci. Eng.* **24**, 055007 (2016).
34. C. Lu *et al.*, Direct observation of defect range and evolution in ion-irradiated single crystalline Ni and Ni binary alloys. *Sci. Rep.* **6**, 1–10 (2016).
35. D. S. Aidhy *et al.*, Point defect evolution in Ni, NiFe and NiCr alloys from atomistic simulations and irradiation experiments. *Acta Mater.* **99**, 69–76 (2015).
36. M. W. Ullah, D. S. Aidhy, Y. Zhang, W. J. Weber, Damage accumulation in ion-irradiated Ni-based concentrated solid-solution alloys. *Acta Mater.* **109**, 17–22 (2016).
37. Z. Su *et al.*, Radiation-assisted chemical short-range order formation in high-entropy alloys. *Scripta Mater.* **212**, 114547 (2022).
38. L. Koch *et al.*, Local segregation versus irradiation effects in high-entropy alloys: Steady-state conditions in a driven system. *J. Appl. Phys.* **122**, 105106 (2017).
39. P. Olsson, C. Domain, J. Wallenius, Ab initio study of Cr interactions with point defects in bcc Fe. *Phys. Rev. B* **75**, 014110 (2007).
40. B. Xing, X. Wang, W. J. Bowman, P. Cao, Short-range order localizing diffusion in multi-principal element alloys. *Scripta Mater.* **210**, 114450 (2022).
41. Z. Su *et al.*, Enhancing the radiation tolerance of high-entropy alloys via solute-promoted chemical heterogeneities. *Acta Mater.* **245**, 118662 (2023).
42. H. Mehrer, *Diffusion in Solids: Fundamentals, Methods, Materials, Diffusion-Controlled Processes* (Springer Science & Business Media, 2007).
43. E. Ma, Unusual dislocation behavior in high-entropy alloys. *Scripta Mater.* **181**, 127 (2020).
44. E. Ma, X. Wu, Tailoring heterogeneities in high-entropy alloys to promote strength-ductility synergy. *Nat. Commun.* **10**, 5623 (2019).
45. T. Shi *et al.*, Distinct point defect behaviours in body-centered cubic medium-entropy alloy NbZrTi induced by severe lattice distortion. *Acta Mater.* **229**, 117806 (2022).
46. S. Plimpton, Fast parallel algorithms for short-range molecular dynamics. *J. Comput. Phys.* **117**, 1–19 (1995).
47. B. Sadigh *et al.*, Scalable parallel Monte Carlo algorithm for atomistic simulations of precipitation in alloys. *Phys. Rev. B* **85**, 184203 (2012).